Effect of manufacturing strategy on the toughness behavior of Inconel 625 laser metal deposited parts

Davide Verdi[1*], Naresh Varadaraju[1], Eddie Tan Zhi'En[1,2], Alin Patran[1]

[1] Agency for Science, Technology and Research (A*STAR), Advanced Remanufacturing and Technology Centre (ARTC), 3 CleanTech Loop, CleanTech Two, #01/01, 637143 Singapore

[2]Nanyang Technological University (NTU), School of Mechanical and Aerospace Engineering, 50 Nanyang Ave, 639798 Singapore

* Corresponding author: (E) davide_verdi@artc.a-star.edu.sg (T) +65 8324 5256

Abstract

Nickel based superalloys are broadly used to produce high value added components in industrial sectors like oil and gas, aerospace, energy production, etc. Additive manufacturing represents a viable alternative family of processes for near-net shape fabrication. This paper presents results related to the toughness behavior of laser metal deposited Inconel 625 samples under impact tests, in the as-deposited and post heat treated condition. Laser metal deposition was used to build Inconel 625 Charpy impact tests samples in two different orientations: vertical and horizontal. Half of the samples for each build orientation were subjected to annealing heat treatment while the remainder were kept as-built. Distinct toughness behaviors were observed, with the vertical builds exhibiting a higher absorbed energy than the horizontal one. Furthermore, a decrease in absorbed energy after heat-treatment was observed in the Charpy impact test results for both deposition orientation samples. A similar behavior was observed through Vickers microhardness measurements. However, in this case, while the horizontal deposited samples resulted always harder than the vertical ones, the heat treatment reduced the hardness difference between the two deposition directions. The obtained results highlight the influence of the manufacturing strategy on the toughness of the final components.

Keywords: Inconel 625; toughness; Charpy impact test; laser metal deposition; directed energy deposition; heat treatment; Vickers hardness

1. Introduction

Inconel 625 (IN625) is a Ni-based superalloy commonly used to manufacture high added value components due to its outstanding mechanical properties, at both cryogenic and high temperature, as well as its excellent resistance to different corrosive media, as reported by several authors such as Rombouts, et al. [1], Hong, et al. [2], Olakanmi et al. [3], and Abioye et al. [4]. For example, IN625 is used in the oil and gas sector for components subjected to high mechanical stresses in sea water, components exposed to flue gas, or flare stacks on offshore oil platforms [5][6]. Leyens & Beyer [7] also reported applications of IN625 in the energy

production industrial sector while Gasser, et al. [8] highlighted its application in the aerospace sector. However, as reported by Choudhury & El-Baradie [9], its relatively high cost in comparison with more commonly used stainless steels, as well as its higher hardness, higher mechanical properties, and lower thermal diffusion – all of these making it difficult to machine – restrict its use.

Different authors, such as Leino, et al. [10] and Mahamood, et al. [11], pointed-out how Laser Metal Deposition (LMD), an Additive Manufacturing (AM) process in the Directed Energy Deposition (DED) family, represents nowadays a valid solution to avoid material wastage and reduce production costs via remanufacturing. In LMD, a laser beam is used as energy source to melt a feedstock material, in form of powder or wire, and deposit it on a substrate. As described by Selcuk [12], the laser beam melts also a small amount of the substrate surface, and the base material will be mixed with the deposited one, generating a strong metallurgical bond. With LMD it is possible to reduce the amount of material to be machined by building near net shape components, consequently decreasing costs and wastages. Another use of the LMD is to repair damaged components, increasing in this way the effective service life of a part, as reported by Graf, et al. [13] and Binger, et al. [14].

By using the LMD with IN625, it is possible to achieve near-fully dense final products. For example, Zhong et al. [15] reported a porosity of 0.009% measured in a single track deposition. Fujishima et al. [16] reported values of porosity that vary between 0.005% and 0.040% obtained by varying LMD key process parameters such as laser power, powder flow, or carrier gas, while depositing single lines and thin-walled structures. Other authors like Kim & Saldana [17] reported values of porosity between 0.2% and 1.0% in thin-walled IN625 structures obtained with different laser powers.

Additively built components exhibit strong mechanical and microstructural anisotropic properties, largely in relation to the build orientation. Rombouts et al. [1] reported a preferential dendritic growth parallel to the build direction in IN625, leading to a lower yield strength when loaded along the build direction. Selcuk [12] also observed similar anisotropic behaviors in numerous materials built by LMD, including IN625. Wang et al. [18] demonstrated that in LMD built IN625 parts, the grain growth is primarily driven by the laser-induced heat flow direction, perpendicular to the laser scanning direction, which generates a strong directional microstructure. Similarly, Dinda et al. [19] showed that as-deposited LMD built IN625 consists of mostly columnar dendrites that grow epitaxially from the substrate.

In addition, a number of studies have investigated LMD built IN625 parts' impact resistance properties via Charpy impact test under various conditions. Puppala et al. [20] demonstrated that

the stress-relieving heat treatment on LMD built IN625 Charpy impact samples produced a slight increase in the impact energy from 48 - 50 J to 50 - 54 J. Paul et al. [21] found that LMD built IN625 samples have comparable impact resistant properties to conventional processes while maintaining ductile properties.

However, the toughness behavior under impact tests of LMD IN625 parts in relationship to the samples manufacturing strategy was not reported in literature. This paper is addressing this gap, by presenting a comparison of the behavior before and after heat treatment and a correlation with the microstructure.

2. Materials and Methods

The IN625 samples were built using raw material in powder form which was provided by voestalpine BÖHLER Edelstahl GmbH. & Co. KG (Kapfenberg, Austria). The product is commercially known as BÖHLER L625 AMPO (https://www.bohler-edelstahl.com/en/additive-manufacturing/) and its composition is shown in Table 1. In the table, both compositions, as per AMS 5666 standard (nominal) and as reported in the manufacturer Certificate of Conformance (measured, via inductively coupled plasma atomic emission spectrometry as per ASTM E2594, and combustion analysis as per ASTM E1019), are included. The powder is prepared by gas atomization and it is offered with particle size distribution (PSD) between 45 µm and 150 µm. A flowability of less than 21 s (ISO 4490:2014) and an apparent density of 3.5 g/cm^3 (ISO 3923-1:2018) are also specified by the manufacturer.

Table 1: Chemical composition of BÖHLER L625 AMPO powder

	Element, wt. %								
	C	Cr	Mo	Ni	Co	Ti	Al	Nb	Fe
Nominal	0.050 max.	21.00	8.50	Bal.	1.00 max.	0.40 max.	0.40 max.	3.40	5.00 max.
Measured	0.015	21.36	8.11	Bal.	0.13	0.07	0.29	3.33	3.64

Prior to utilizing the powder for the deposition of the samples, an internal powder quality check was carried out to confirm the information provided by the manufacturer. In addition, the porosity contained in the powder particles was measured. Powder samples were mounted in resin and polished to observe their cross section and analyze the average powders' pores percentage (area %). According to the ISO 13322-1 standard, for statistical significance, a minimum of 10,000 particles were counted. For this goal, images of the particles cross sections were taken by means of an optical microscope Zeiss AxioScope coupled with the image processing software AxioVision. The image stitching tool was used to create a single picture

formed by 25 images captured at higher magnification (x200). In this way, objects with a minimum dimension of 0.314 μm and an area of 0.0494 μm^2 can be identified.

Alloy 825 (EN NiCr21Mo) plates of dimensions 300 × 300 × 15 mm^3 of were used as substrates for the deposition. The plates were again provided by voestalpine BÖHLER Edelstahl GmbH. & Co. KG (Kapfenberg, Austria), the material being commercially known as BÖHLER L314 (https://www.bohler-edelstahl.com/en/products/l314/). The nominal (as per ASTM B424 standard) and measured (via inductively coupled plasma atomic emission spectrometry as per ASTM E2594, and combustion analysis as per ASTM E1019) chemical composition reported by the manufacturer in the material inspection certificate of the plates is shown in Table 2.

Table 2: Chemical composition of BÖHLER L314 plates

	Element, wt. %						
	C	Cr	Mo	Ni	Cu	Ti	Fe
Nominal	0.025 max	21.50	3.00	40.00	2.30	0.90	Bal.
Measured	0.013	21.99	3.02	38.50	1.59	0.72	Bal.

The samples deposition was carried out in the Advanced Remanufacturing and Technology Centre (ARTC) by using a DMG MORI Lasertec 65 3D Hybrid machine. A coaxial powder nozzle COAX-9 (Fraunhofer Institute for Material and Beam Technology IWS) was used. A total of 32 samples were deposited, 16 of them in vertical (V) direction, of square base of 15 mm × 15 mm and a total height of 70 mm, and the other 16 in horizontal (H) direction, with a rectangular base of 60 mm × 15 mm and height of 25 mm. A schematic view of the samples and their dimensions can be seen in Figure 1. These dimensions were chosen based on the size of the samples to be machined for the Charpy impact tests.

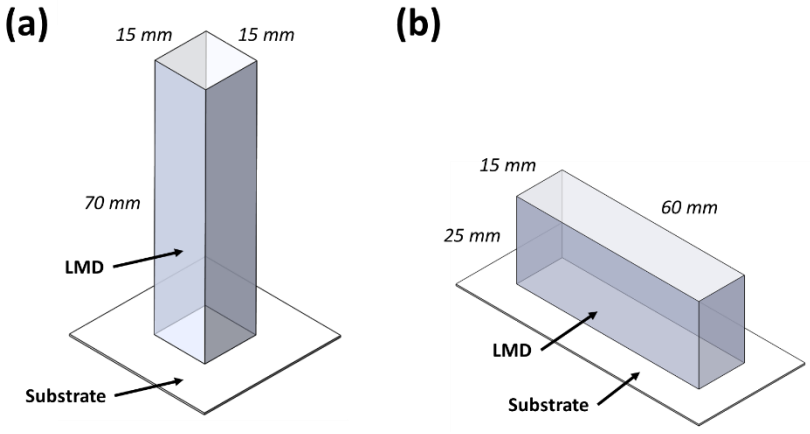

Figure 1: Schematic view for (a) vertical and (b) horizontal orientation builds

The samples were cut 10 mm above the substrates to avoid the interaction between the deposited and the base materials (i.e. IN625 alloy composition change due to dilution with substrate material). For each deposition direction, six samples were used for microhardness measurements, as described in more detail in the following sections.

The same LMD parameters were used to deposit the samples in both vertical and horizontal orientations. A laser spot size of 1.6 mm was used while Argon was employed as process gas. The levels of the different parameters used (i.e. laser beam power, scanning speed, powder mass flow rate, carrier gas flow, shielding gas flow) were selected through a parameter selection process. Due to a confidentiality agreement with the industrial partner voestalpine Additive Manufacturing Center Singapore Pte. Ltd. (vAMCS), these parameters cannot be disclosed. For both geometries a 0°/90° deposition strategy without contours was used, as schematized in Figure 2.

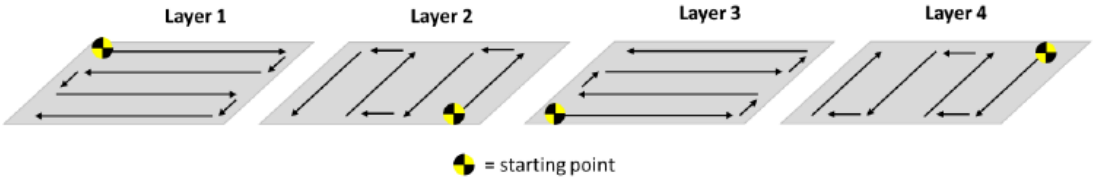

Figure 2: LMD deposition strategy

Six vertical and six horizontal samples were subjected to heat treatment before being cut for microhardness tests or machined for Charpy impact tests. A total of four experiment conditions were therefore obtained: vertical build orientation – non-heat-treated (V+NHT); vertical build orientation – heat-treated (V+HT); horizontal build orientation – non-heat-treated (H+NHT); and horizontal build orientation – heat treated (H+HT). The heat treatment undergone was an annealing process, done in accordance with the AMS 5666 standard: the samples were heated up to 885°C where they were held for 1 hour before rapidly cooling in air to room temperature. The heat treatment was carried out in an air circulated furnace. This heat treatment is a requirement for forged and rolled IN625 in aerospace and oil and gas sectors. Through this process it is possible to achieve a compromise among recrystallization, precipitation of carbides, and stress relief. As reported by Ghate et al. [22], the annealing of IN625 is commonly done at temperatures that range from 700°C to 1200°C, where 870°C represent the most common stress-relieve temperature. However, as highlighted by Stoudt et al. [23], a higher annealing temperature helps to homogenize faster the microstructure after the LMD. For such reason, the temperature of 885°C was selected in this work.

Metallographic samples were extracted from the tested Charpy impact specimens, hot mounted, polished, and chemically etched for two minutes using the mix number 94 (Kalling's No. 2 reagent) listed in the ASTM E407 standard. The sectioned and measurement surface locations are illustrated in Figure 3.

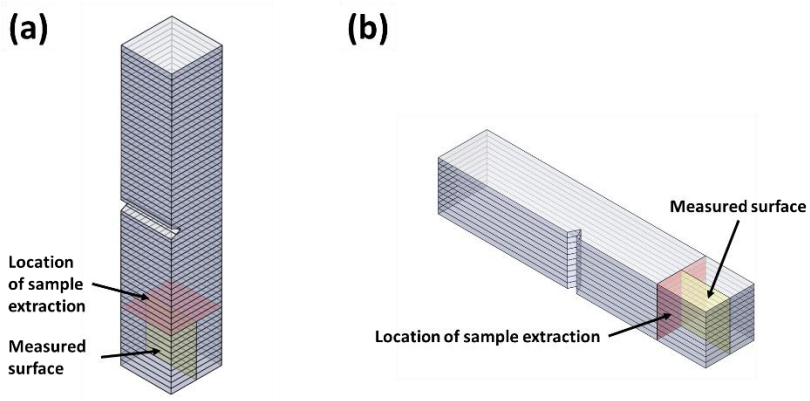

Figure 3: Metallographic samples extraction from Charpy impact coupons for (a) vertical and (b) horizontal orientation build

The internal porosity of the LMD builds was measured by analyzing optical microscope images taken before etching. The Zeiss AxioScope microscope, coupled with the AxioVision image processing software were again used. Grain size measurements were done in accordance to the ASTM E112-13's standard Abrams Three-Circle procedure. This method was chosen due to its compensation for non-equiaxed grain structures, typically observed for LMD builds as reported by Dinda, et al. [19]. The procedure consists in applying a pattern, made of three concentric and equally spaced circles with a total circumference of 500 mm, to at least five areas sufficiently spaced of the same sample. Subsequently, the operator has to manually count the intersections of the circles with the grain boundaries. The number of intercepts (N) or the number of grain boundary intersections (P) per unit length of test line are then calculated as a function of the length of a test line and the magnification used. The mean lineal intercept length (l), that correspond to the grain size, is then calculated as a function of N or P. As specified by the ASTM E112-13, the magnification of the micrographs has to be selected to assure at least 40-100 intercepts per image (at least 500 counts per sample). In the current work, a magnification of x50 was chosen.

Five high magnification (x500) optical microscope images were taken for each test condition (V+NHT, H+NHT, V+HT, and H+HT) to measure the dendrite arm spacing (DAS). Areas of 13000 μm^2 were selected and analyzed in each micrograph using the Fiji open-source software (https://fiji.sc/). The DAS was determined using the Kurz-Fisher model [24]:

$$\lambda = N^{-1/2} \quad (1)$$

where λ represents the DAS and N the numbers of dendrites cores per unit of area. To derive N, the number of cores measured within the bounding rectangle is divided by the area of the bounding measurement rectangle. Finally, to study the effects of the build orientation and the heat treatment on secondary phases, a Scanning Electron Microscopy (SEM) analysis was carried out using the Zeiss EVO HD 25 microscope equipped with an energy dispersive X- ray microanalyser (EDX). Secondary (SE) and backscattered (BSE) electron images were captured for each experiment condition. Image analysis was performed on five SE images of each condition to quantify the amount of secondary phases. Thresholding was applied for each image to isolate and identify the secondary phases. Once again, the open-source software Fiji was used to measure the area percentage of secondary phases in each image.

Charpy impact and Vickers microhardness were used as tests methods to characterize the deposited LMD samples and study the effects of the deposition strategy and heat treatment on their behavior. Charpy impact tests were conducted at room temperature in accordance to ASTM E23-18 to determine the toughness of the LMD specimens. From the Charpy tests, the absorbed energy and the lateral expansion values were recorded. The specimens used in this study were the V-shaped notch type with dimensions of 10 mm × 10mm × 55 mm, illustrated in Figure 4. The V-notch type specimen was used to ensure the control of the stress concentration by the location of the minimum cross-section area, therefore controlling the fracture behavior.

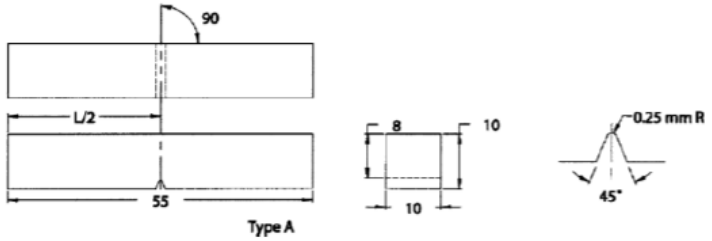

Figure 4: Charpy impact test samples dimensions

One specimen was extracted from each of the LMD builds. Five samples per experiment condition (V+NHT, H+NHT, V+HT, and H+HT) were machined and tested. Vickers microhardness tests were conducted in agreement with the ASTM E384 standard. The measurements were carried out on three samples for each tested condition, before machining. The tested area, of about 60 mm × 15 mm, was mirror-like polished and etched using the mix number 94 (Kalling's No. 2 reagent) from the ASTM E407 standard for 2 minutes, as mentioned before. An Innova Test Falcon 500 microhardness tester was used. A load of 500 gf and a 10

seconds dwell time were selected to conduct the microindentation measurements. Three rows of 20 microindentations were taken across three samples for each experiment condition: V+NHT, H+NHT, V+HT, and H+HT. An indentation spacing bigger than 5d, where d represents the diameter of the equivalent indentation mark, were used in agreement with the recommendation of the ASTM E384 standard. The microindentation locations are schematized in Figure 5 and were designed in such way to cover all the 60 mm × 15 mm areas. The diagonals of the indentation marks were measured using the x40 magnification of the indenter optic system.

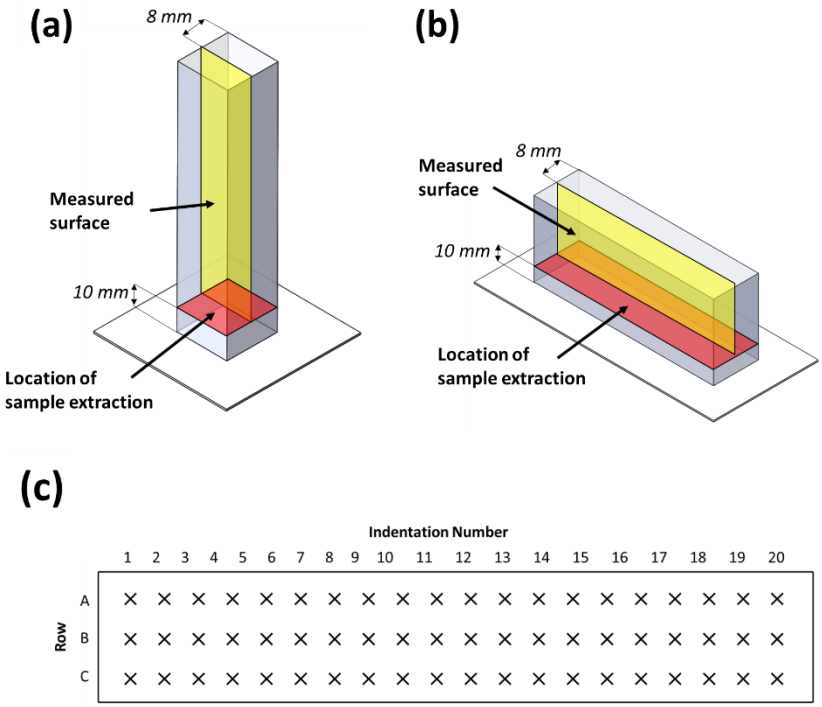

Figure 5: Vickers microindentation locations. Schematic view of the measured surface for (a) vertical and (b) horizontal samples, and (c) test locations with indication of rows and indentation numbers

3. Results and Discussion

As mentioned, an internal powder quality check was performed before loading the powder in the LMD machine. The actual PSD was measured as per ISO 13322-2 and the results are as follows: D10 = 53.0 µm, D50 = 91.9 µm, D90 = 133.1 µm, where the reported values represent the size under which the 10%, 50%, and 90% of the analyzed particles fall respectively. Figure 6a and Figure 6b show two SEM-SE images of the powder, in which the mixed morphology of the particles (spherical, elongated, irregular, and satellited) typical of gas atomized powders can be observed. Figure 6c shows an example of optical microscope image used for the characterization of the powder particles porosity percentage. Based on the measurements done

on 40,526 particles, 26,697 pores were detected and a porosity (area %) of 0.593% was measured.

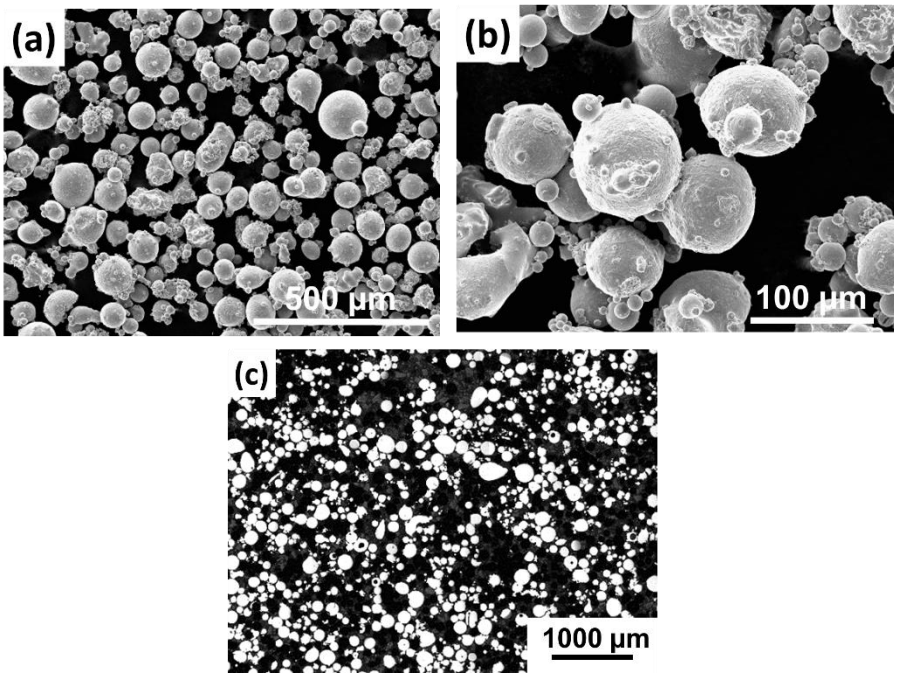

Figure 6: SEM-SE images of L625 AMPO powder: (a) x100, and (b) x350 magnifications. (c) Example of optical microscope image of the L625 AMPO powder cross section

Figure 7 shows two examples of the as-deposited samples, one for each build direction. No particular issues were encountered during the deposition, and the obtained builds had dimensions close to the programmed ones shown in Figure 1. The build efficiency (i.e. mass of blown powder vs. mass of the final build) was calculated to be around 70%.

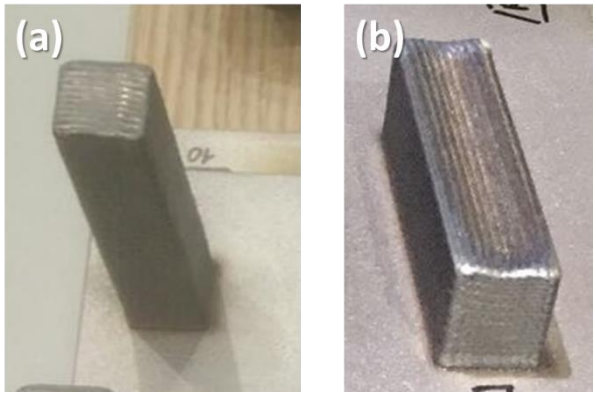

Figure 7: Example of as-deposited samples, (a) vertical, and (b) horizontal builds

An average porosity of 0.197 ± 0.056% and 0.236 ± 0.048% was measured respectively in the vertical and the horizontal builds, on the metallographic samples extracted as schematized in Figure 3. These values are more than 50% smaller than the porosity measured in the L625 AMPO raw powder. This result highlights the proper selection of the LMD parameters that

permitted the deposition of parts with low porosity and other major defects. As mentioned in this introduction section, a wide range of porosity values are reported in literature for LMD IN625 builds. The levels achieved in this work are low in comparison – as an example, those reported by Kakinuma et al. [25] measured values of 0.244 and 0.787 in 3 mm thick walls IN625 builds, using a powder with PSD of 45-120 µm. As mentioned by the authors in the article, with smaller powder particles it is most probable to obtain lower values of porosity [25]. Marchese et al. [26] reported porosity values of 0.10% - 0.25%, measured in LMD IN625 cubes with dimensions of 15 × 15 × 15 mm^3, starting with a powder with intrinsic porosity of 0.21%.

Micrographs of the grain structures for each condition are shown in Figure 8. As highlighted as an example in Figure 8a, distinct deposition track boundary regions are observable in the micrographs, indicating the adjacent perimeters of the deposition tracks or layers' melt pools. Columnar grain structures are observed to grow epitaxially from the substrate (along the deposition direction). Comparing the vertically built samples with the horizontally built ones, no significant differences in the dimension and orientation of the grains can be observed.

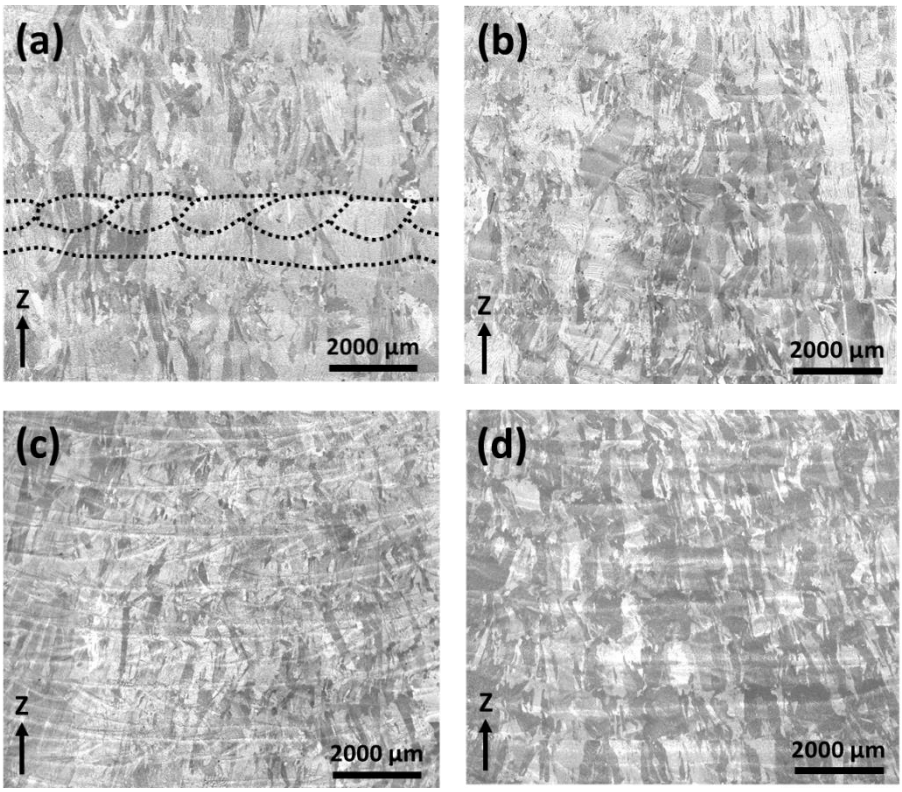

Figure 8: Microstructure micrographs of grains for (a) V+NHT, (b) H+NHT, (c) V+HT, and (d) H+HT. The Z-axis represents the deposition direction.

The measured mean grain sizes are listed in Table 3. Similar values were reported by other authors. For example, Dinda et al. [19] reported mean values of approximatively 250 µm and 100 µm in the core and edges of 8 mm thick thin-walled IN625 LMD builds respectively. The

observed columnar microstructure is the result of the process heat flow direction which is preferentially parallel to the vertical build direction. The grain sizes measured for the as-built vertical samples (V+NHT) are comparable with the horizontal ones (H+NHT). The mean grain size dimensions for the specimens exposed to annealing treatment (V+HT and H+HT) are higher than those in the as-built condition. However, comparing the minimum and maximum dimensions, as well as the percentiles (D10, D50, and D90) values reported in Table 3, it is possible to assert that the heat treatment did not significantly affect the grain structure of the samples.

Table 3: Abrams three-circle procedure grain size measurement results for V+NHT, H+NHT, V+HT, H+HT conditions

Condition	**Mean (µm)**	**Min (µm)**	**Max (µm)**	**D10 (µm)**	**D50 (µm)**	**D90 (µm)**
V+NHT	190	27	863	66	146	412
H+NHT	174	30	767	124	146	372
V+HT	230	56	536	108	212	370
H+HT	221	47	751	98	190	384

Examples of the micrographs used to measure the DAS for each condition are shown in Figure 9. Two distinct main phases can be observed from these images: the dendrite core regions (brighter areas in the images) and the secondary phases (darker and irregularly dispersed).

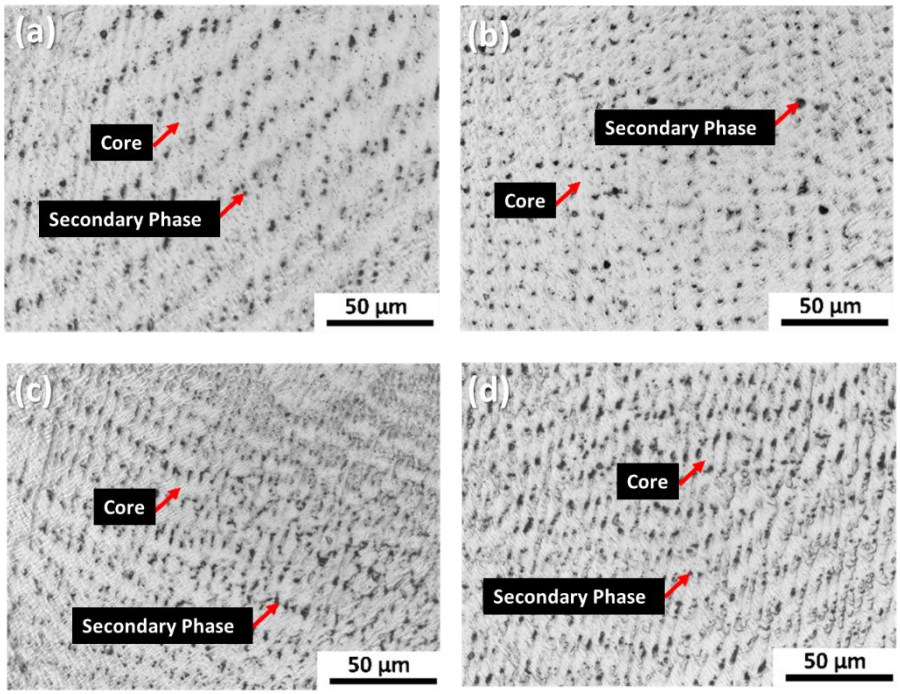

Figure 9: High magnification micrograph showing microstructure of secondary phases and cores for (a) V+NHT, (b) H+NHT, (c) V+HT, and (d) H+HT

The average DAS measurements results made across five micrographs are summarized in Table 4. The DAS are derived from the number of mean cores per unit area using Eq. (1). In all cases, the mean DAS were found to be around 12 – 13 µm. These results highlight the fact that both vertical and horizontal builds underwent quasi-equivalent thermal histories during deposition. In addition, the heat treatment did not significantly affect these microstructural characteristics. Similar results were reported by other authors. For example, Zhang et al. [27] measured a primary DAS of approximatively 10 µm in graphite reinforced IN625 obtained by LMD. DAS between 8 and 12 µm were also mentioned by Huang et al. [28] in LMD IN625 samples obtained at different scanning speeds. The same authors reported a correspondent cooling rate, simulated and confirmed to be of the order of 10^2 – 10^3 K/s. This results agree with Mehrabian's observations made on another Ni-based superalloy (Inconel 718) [29] and the relationship between cooling rate and DAS proposed by Davies et al. [30]:

$$\lambda = (97 \pm 5)\left(\frac{\Delta T}{\Delta t}\right)^{-0.36\pm0.01} \quad (2)$$

where λ represents the DAS and $\Delta T/\Delta t$ the cooling rate.

Table 4: Mean DAS results

Condition	Mean DAS (µm)
V+NHT	12.4 ± 0.3
H+NHT	12.1 ± 0.4
V+HT	12.7 ± 0.3
H+HT	12.6 ± 0.3

Figure 10 shows low magnification SEM-SE images of samples of the four experiment conditions. No significant differences can be identified among the four images, highlighting again a very similar microstructure among samples deposited vertically and horizontally, as well as before and after the annealing treatment. The SEM-SE images reported in Figure 11 show the presence of secondary phases in the interdendritic regions and along the grain boundaries in both as-deposited and heat treated IN625 LMD microstructures.

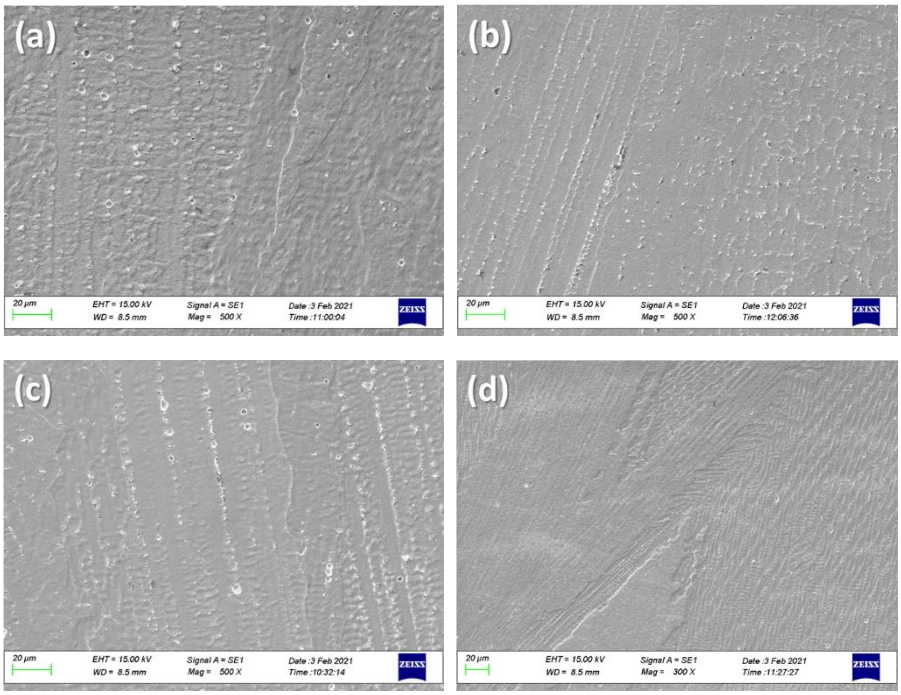

Figure 10: Low magnification SEM-SE image of (a) V+NHT, (b) H+NHT, (c) V+HT, and (d) H+HT specimens

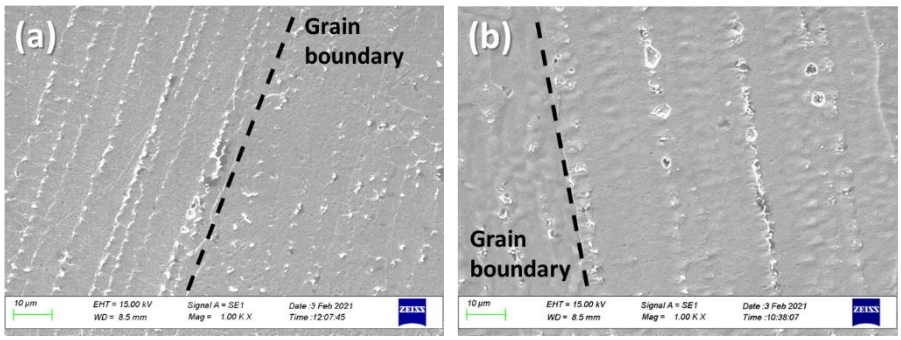

Figure 11: SEM-SE images of LMD IN625 samples, (a) as-deposited and (b) after heat treatment, showing secondary phases in interdendritic regions and grain boundaries

The microstructures of the as-deposited and heat treated samples were further analyzed. Higher magnification SEM images of the as-deposited IN625 microstructure are illustrated in Figure 12. The presence of irregular shaped particles (marked with 2 in Figure 12b) and other more regular or rounded ones (marked with 3 in Figure 12b) can be observed in the γ-Ni matrix of the IN625 (Figure 12c). The EDX analysis showed that, with respect to the γ-Ni, the irregular shaped particles have a higher content of Mo, Nb, and Si (Figure 12d), while the smaller round ones are richer in Nb and Mo, and contain traces of Ti (Figure 12e). Different authors such as Rombouts et al. [1], Silva et al. [31], Dubiel et al. [32], and Verdi et al. [33], identified the first as Laves phase, with hexagonal crystal structure and composition type AB_2 of general formula $(Fe,Cr,Mn,Si)_2(Mo,Ti,Nb)$. The formation of this phase is promoted by the presence of Si and Nb in the alloy[1]. The same authors identified the smaller particles as metallic carbides. Among the four types typically observed in Ni-based superalloys (MC, M_6C, M_7C_3, and $M_{23}C_6$), Ti and Nb rich MC with a globular or cubic form, and Mo rich M_6C with blocky shape or Widmanstätten pattern, are the most common [34].

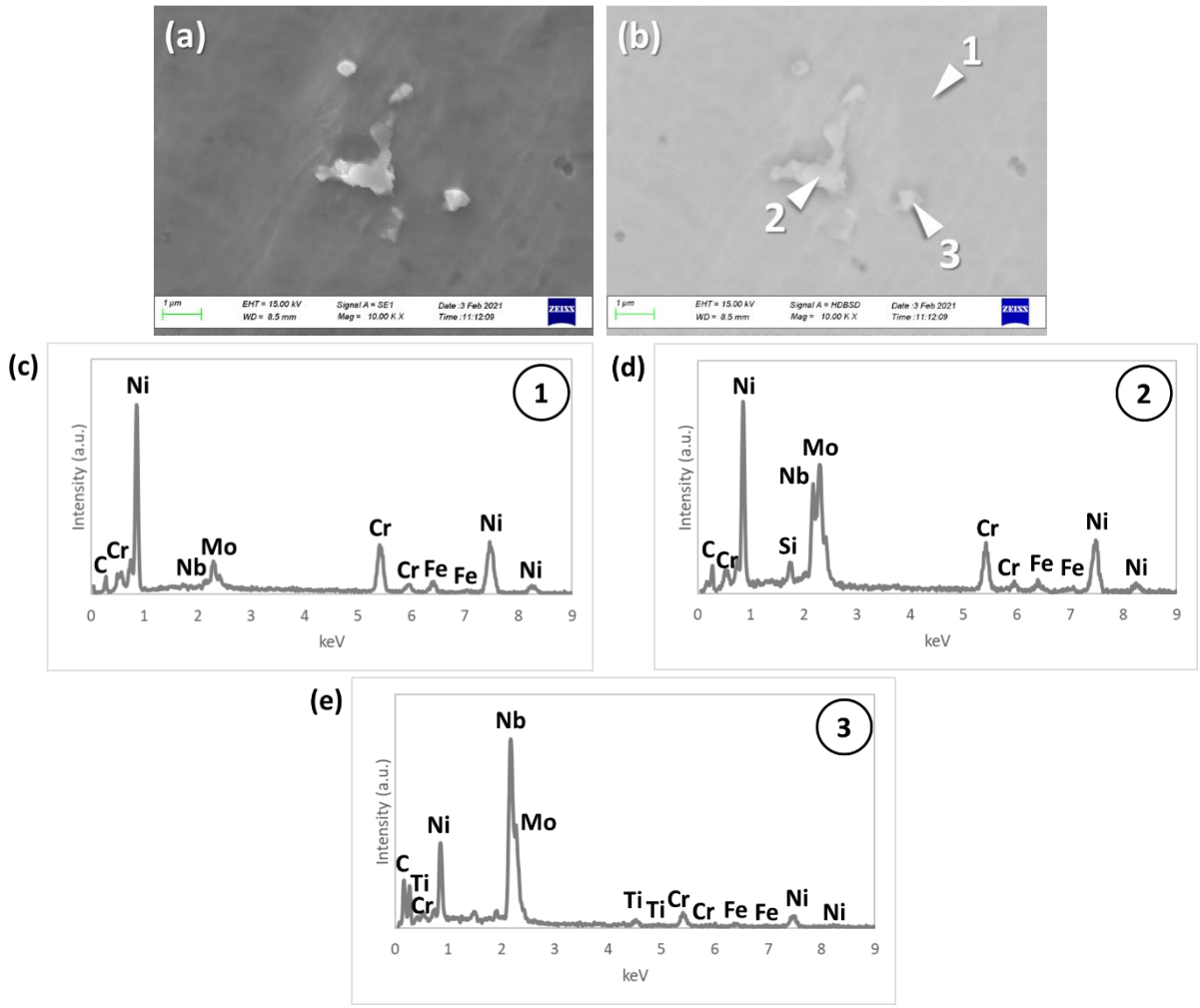

Figure 12: SEM (a) SE and (b) BSE images showing the secondary phases observed in the as-deposited IN625 samples. (c-e) EDX spectra of phases pointed out in the BSE image

In Figure 13 higher magnification SEM images of the annealed IN625 LMD samples are reported. The presence of numerous secondary phases can be observed again in the γ-Ni matrix (Figure 13c). While the bigger and irregular shape particles can be identified once more as Laves (Figure 13d) and the smaller rounds ones as Nb-rich MC (Figure 13d), the very occasional presence of elongated / acicular phases was observed (marked with 4 in Figure 13b). Despite their morphology suggesting the formation of δ-Ni_3Nb phase as precipitation of the metastable γ”-Ni_3Nb during heat treatment [34], the result of the EDX analysis on such particle (Figure 13e) showed no differences with Laves phase. However, due to the small size of the observed particles (less than 1 µm), it is only possible to speculate that δ-Ni_3Nb phase formed during the heat treatment, based on the time-temperature-transformation (TTT) diagrams for additive manufactured IN625 reported by other authors [23]. On the other hand, as previously mentioned for the as-deposited samples, these elongated particles could also be classified as M_6C type carbides.

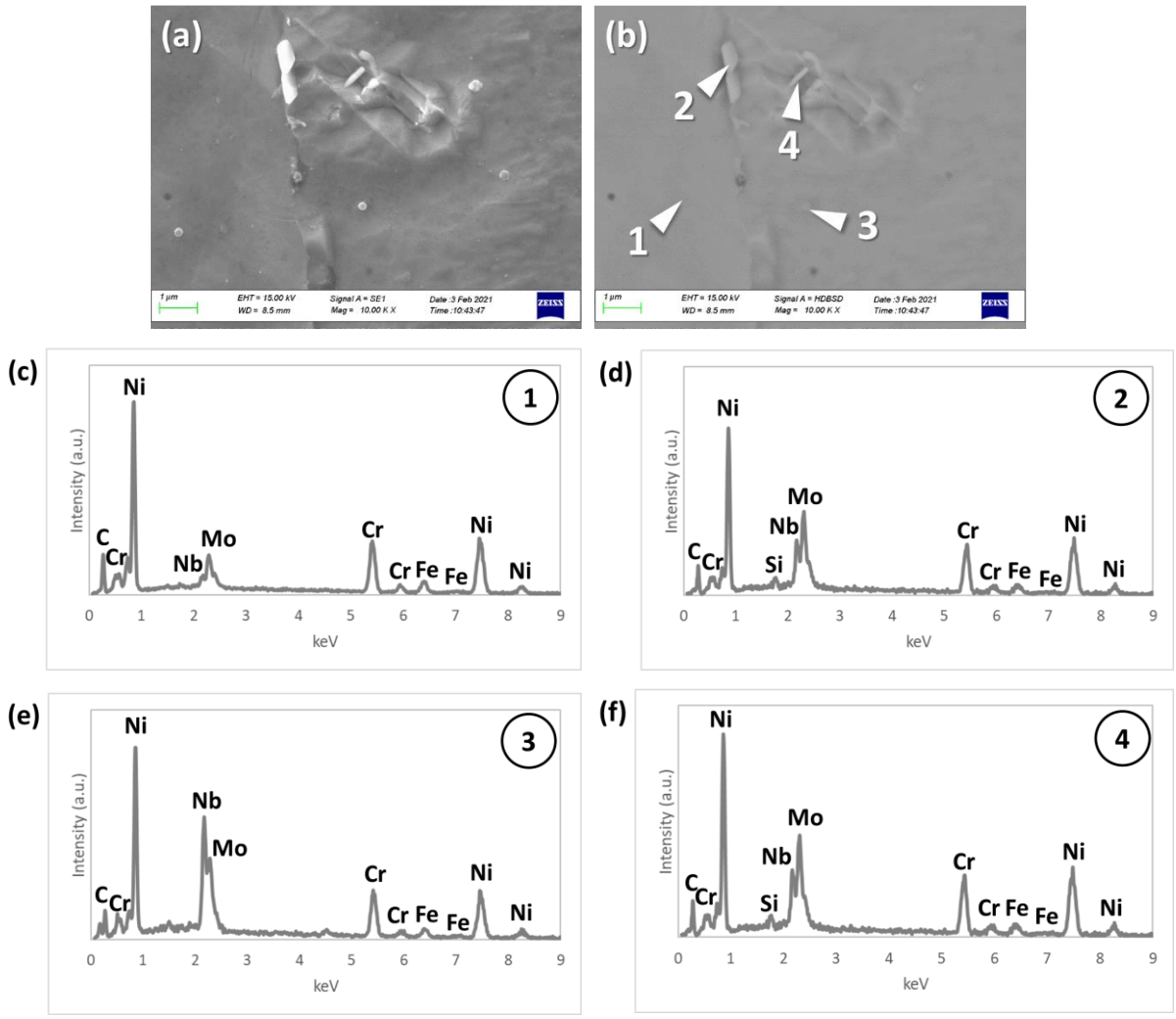

Figure 13: SEM (a) SE and (b) BSE images showing the secondary phases observed in the heat treated IN625 samples. (c-f) EDX spectra of phases pointed out in the BSE image

As also reported by other authors [1], the complete identification of the different phases formed in rapidly solidified IN625 needs additional analysis techniques, such as Transmission Electron Microscopy (TEM), which were not included in the present research project.

The secondary phase measurement results are summarized in Table 5. No significant differences were observed neither in secondary phases' content between samples deposited in different orientations, nor before and after exposure to the annealing treatment.

Table 5: Contents in area percentage of secondary phases

Condition	Secondary phases (area %)
V+NHT	2.79 ± 0.57
H+NHT	3.34 ± 0.62
V+HT	2.60 ± 0.70
H+HT	2.82 ± 0.81

The results from the Charpy impact tests (average absorbed energy and lateral expansion) for each of the tested conditions are reported in Table 6. The results show approximately 15% less absorbed energy and 4% less lateral expansion for the as-deposited horizontal build orientation samples (H+NHT) when compared to the vertical ones (V+NHT). In both cases, the LMD built IN625 showed a relatively high ductile behavior, absorbing approximately 50% of the initial energy (300 J). In opposition to the expected effect, the annealing treatment in this case had the effect of slightly reducing the ductile behavior of the samples. For the vertical builds (V+NHT vs. V+HT) a 15% reduction of the absorbed energy was measured, with a reduction of about 20% for the horizontal samples (H+NHT vs. H+HT). A difference of about 21% was calculated between the vertical and the horizontal samples after heat treatment. The lateral expansion also decreases after annealing (by 4% for the vertical builds and by 12% for the horizontal ones), with a difference of about 21% calculated between V+HT and H+HT conditions.

Table 6: Charpy impact tests results

Condition	Mean absorbed energy (J)	Mean lateral expansion (mm)
V+NHT	162 ± 10	2.23 ± 0.10
H+NHT	137 ± 2	1.90 ± 0.09
V+HT	138 ± 6	2.13 ± 0.07
H+HT	109 ± 2	1.68 ± 0.06

Similar values of absorbed energy, obtained via Charpy impact tests, were reported by other authors. For example, Silva et al. [31] measured an impact strength of 141.3 ± 14.3 J on IN625 welded coatings while Thomas & Tait [35] stated a value of 178 J obtained from samples extracted from a wrought IN625 component. Floreen et al. [36] reported iso-Charpy V-notch energy curves for different annealing times and temperatures; for exposure times less than 10 hours, an absorbed energy around 150 J is reported.

The graph in Figure 14 presents, for each sample, the average of three hardness values for each indentation point (1 to 20) obtained averaging the results of the three rows illustrated in Figure 5 (e.g. indentation number 1 in Figure 14 was obtained averaging the results from the indentations 1A, 1B, and 1C). It can be seen that for each condition separately, the hardness values measured are relatively consistent across the LMD builds, from top to bottom for vertical builds, and from left to right side for the horizontal ones. As a consequence, a mean hardness value for each tested condition was calculated (average of 60 indentations).

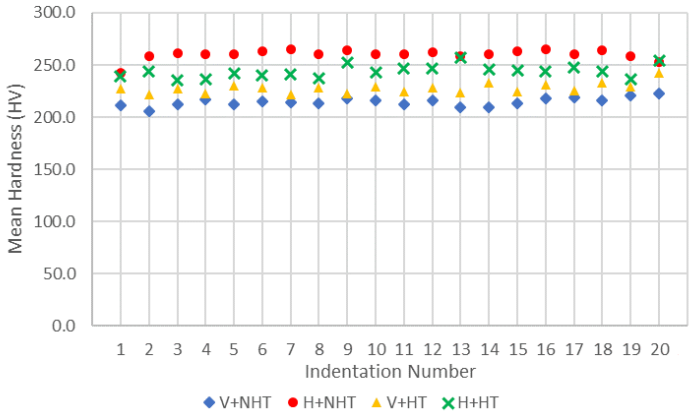

Figure 14: Mean hardness results per indentation number for V+NHT, H+NHT, V+HT, H+HT conditions

The calculated hardness values are summarized in Table 7. It can be seen that the H+NHT condition hardness is about a 17% higher with respect to the V+NHT condition. After the annealing treatment, the horizontal builds hardness remained higher, but the difference with respect to the V+HT was reduced to about 6%. After the heat treatment the average hardness for the vertical builds increases by about a 6%, while for the horizontal builds decreases by about 7%.

Table 7: Hardness measurements results

Condition	**Mean hardness ($HV_{0.5}$)**
V+NHT	214.7 ± 6.8
H+NHT	260.1 ± 7.4
V+HT	227.8 ± 11.1
H+HT	243.8 ± 13.9

For comparison, Rombouts et al. [37] showed that LMD built IN625 annealed at >800 °C exhibits a drop in hardness values independently from the deposition direction (vertical or horizontal).

The authors attributed this trend to the decomposition of the MC carbides, originally present in the as-deposited specimen, to $M_{23}C_6$ and M_6C after exposure to high temperatures.

The tests results showed that the LMD built IN625 samples behavior under impact tests depends on the deposition strategy followed when building the specimens. This behavior can be directly connected to the difference in hardness observed in the different samples. However, relatively small differences in microstructure were identified, suggesting that the observed differences of the mechanical behavior can be related to other factors. IN625 alloy solidification metallurgy is dominated by the segregation to interdendritic regions of elements such as Mo and Nb. In addition, as reported by many authors such as Silva, et al. [38], Chandrasekaran, et al. [39], DuPont & Robino [40], and Kurz & Fisher [41], the alloy solidification process follows three main steps:

$$L + \gamma \rightarrow L + \gamma + MC \rightarrow L + \gamma + MC + Laves$$

An accumulation of secondary phases, such as carbides and Laves, is expected in the interdendritic regions and the grain boundaries. In addition, as reported by Floreen, et al. [36] and Cieslak, et el. [42] the thermal flux is a key factor in determining the directionality of the microstructural grains whereby the grain growth follows the maximum temperature gradient. Selcuk [12] asserts that during the LMD process, where the samples are manufactured layer-by-layer, an elongated columnar grain structure that grows epitaxially from the substrate is expected as the cooling of the melt pool occurs primarily through the previously deposited layer and the substrate. The morphologies and concentrations of the secondary phases are consequently largely dependent on the solidification process during the LMD build. As reported in Table 5, the secondary phases' contents resulted similar independently from the deposition strategy, and the results were not affected by the heat treatment performed.

The bulk hardness properties shown in Table 7 can be related with the brittle intrinsic characteristic of these secondary phases. In fact, a higher hardness value is observed in horizontal built samples, where slightly higher secondary phases' content was observed when compared to the vertical ones. By matching the data collected in Table 6 and Table 7, it is possible to associate higher values of hardness, measured for the H+NHT and the H+HT samples, to a lower amount of absorbed energy (and corresponding lower lateral expansion) measured in the impact tests. By comparing the results of the as-built samples one can see that the V+NHT samples absorbed more energy than the H+NHT ones. In agreement to what was previously mentioned, $HV_{V+NHT} < HV_{H+NHT}$. These relationships remained unchanged after the annealing treatment even if the samples absorbed less energy and the differences in hardness resulted smaller. So, to summarize:

- As-deposited:

    - Absorbed energy: V+NHT > H+NHT
    - Hardness: H+NHT > V+NHT
- After annealing:
    - Absorbed energy: V+HT > H+HT
    - Hardness: H+HT > V+HT

The results can be correlated with the stress relieving effect of the annealing heat treatment process, as reported by Wang, et al. [18]. The secondary phases' contents and the bulk hardness measurements agree also with the Charpy impact tests results. Brittle intermetallic Laves phases generally lead in fact to lower toughness properties. A higher toughness of the samples was observed when the impact works to break the samples in-between layers (vertical builds) then across layers (horizontal builds), as schematized in Figure 3. This can be connected to the presence of secondary phases in the grain boundaries, together with the grains orientation with respect to the load, perpendicular to the deposition direction for the vertically deposited samples, and parallel to the deposition direction for the horizontally built ones (see Figure 8). For the vertical builds the grains are mainly oriented perpendicularly to the notch (to the load). To fracture the specimen, there is a higher amount of hard and brittle phases that have to be broken, as the growing crack will encounter more secondary phases in its path (higher probability to cross a grain boundary). On the other hand, the grains in the horizontal builds are mainly oriented parallel to the notch (to the load) and the crack propagation after impact can follow an easier path through the more ductile γ-Ni matrix of the IN625 (less probability to cross a grain boundary). As a consequence, less energy is absorbed.

In light of these observations, it is possible to assert that the orientation of the layers deposited during the LMD process, with respect to the direction of the impact load, affects the behavior of the LMD built IN625 samples.

4. Conclusions

In this study, the effect of the manufacturing strategy on the toughness behavior of LMD IN625 samples was analyzed through Charpy impact tests, Vickers hardness, and microstructural analysis. Comparisons have been made between samples deposited in two different orientations, horizontal and vertical, and between heat-treated (annealing) and non-heat-treated conditions. The following conclusions were derived:

1. Different toughness properties were observed varying the samples build orientations. The vertical LMD builds exhibited a higher absorbed energy than the horizontal ones. Heat-treated samples showed a lower absorbed energy than the as-built conditions.

2. In agreement with the Charpy impact tests results, different behaviors of the samples were observed also from Vickers microhardness tests. The horizontal built IN625 samples, that showed a lower amount of absorbed energy, measured harder than the vertical ones.
3. The annealing process reduces the hardness difference between vertical and horizontal builds, but the latter remain harder than the vertical ones.
4. The mechanical properties of LMD built IN625 appear to be primarily driven by the brittle characteristics of the secondary phases, identified as Laves and carbides.
5. By depositing the samples in vertical direction, more hard and brittle Laves phases are formed perpendicularly to the impact load. As a consequence, more energy is required to propagate the crack through these phases resulting in a higher toughness of the specimens.

Acknowledgments

The study reported in this paper is part of a wider project, titled "Parameter development and material characterization for laser metal deposition", between the Agency for Science, Technology and Research Singapore – Advanced Remanufacturing and Technology Centre and voestalpine Additive Manufacturing Center Singapore Pte. Ltd. (vAMCS). The authors would like to acknowledge vAMCS and voestalpine AG for the economic support provided through the project.

References

[1] M. Rombouts, G. Maes, M. Mertens, W. Hendrix, *J. Laser Appl.* **2012**, *24*, 052007.

[2] C. Hong, D. Gu, D. Dai, S. Cao, M. Alkhayat, Q. Jia, A. Gasser, A. Weisheit, I. Kelbassa, M. Zhong, R. Poprawe, *J. Laser Appl.* **2015**.

[3] E.O. Olakanmi, K. Malikongwa, S.T. Nyadongo, S. Hoosain, S.L. Pityana, *Surf. Eng.* **2020**, 1.

[4] T.E. Abioye, P.K. Farayibi, A.T. Clare, *Mater. Manuf. Process.* **2017**, *32*, 1653.

[5] V. Shankar, K. Bhanu Sankara Rao, S.L. Mannan, *J. Nucl. Mater.* **2001**.

[6] R.G.N. Silva, A. de S.P. Pereira, J.M.S. de Sousa, M. Pereira, R.H.G. e Silva, *J. Laser Appl.* **2020**.

[7] C. Leyens, E. Beyer, in *Laser Surf. Eng. Process. Appl.*, **2015**.

[8] A. Gasser, G. Backes, I. Kelbassa, A. Weisheit, K. Wissenbach, *Laser Addit. Manuf. Laser Met. Depos. Sel. Laser Melting Turbo-Engine Appl.* **2010**.

[9] I.A. Choudhury, M.A. El-Baradie, *J. Mater. Process. Technol.* **1998**.

[10] M. Leino, J. Pekkarinen, R. Soukka, in *Phys. Procedia*, **2016**.

[11] R.M. Mahamood, E.T. Akinlabi, M.G. Owolabi, **2017**.

[12] C. Selcuk, *Powder Metall.* **2011**.

[13] B. Graf, A. Gumenyuk, M. Rethmeier, *Phys. Procedia* **2012**, *39*, 376.

[14] E.M. Birger, G. V. Moskvitin, A.N. Polyakov, V.E. Arkhipov, *Weld. Int.* **2011**.

[15] C. Zhong, J. Kittel, A. Gasser, J.H. Schleifenbaum, *Opt. Laser Technol.* **2019**.

[16] M. Fujishima, Y. Oda, R. Ashida, K. Takezawa, M. Kondo, *CIRP J. Manuf. Sci. Technol.* **2017**.

[17] M.J. Kim, C. Saldana, *J. Manuf. Process.* **2020**.

[18] Z. Wang, E. Denlinger, P. Michaleris, A.D. Stoica, D. Ma, A.M. Beese, *Mater. Des.* **2017**.

[19] G.P. Dinda, A.K. Dasgupta, J. Mazumder, *Mater. Sci. Eng. A* **2009**, *509*, 98.

[20] G. Puppala, A. Moitra, S. Sathyanarayanan, R. Kaul, G. Sasikala, R.C. Prasad, L.M. Kukreja, *Mater. Des.* **2014**, *59*, 509.

[21] C.P. Paul, P. Ganesh, S.K. Mishra, P. Bhargava, J. Negi, A.K. Nath, *Opt. Laser Technol.* **2007**, *39*, 800.

[22] N.D. Ghate, A. Pandey, A. Shrivastava, in *Miner. Met. Mater. Ser.*, **2020**.

[23] M.R. Stoudt, E.A. Lass, D.S. Ng, M.E. Williams, F. Zhang, C.E. Campbell, G. Lindwall, L.E. Levine, *Metall. Mater. Trans. A* **2018**, *49*, 3028.

[24] W. Kurz, D.J. Fisher, *Acta Metall.* **1981**.

[25] Y. Kakinuma, M. Mori, Y. Oda, T. Mori, M. Kashihara, A. Hansel, M. Fujishima, *CIRP Ann. - Manuf. Technol.* **2016**.

[26] G. Marchese, X. Garmendia Colera, F. Calignano, M. Lorusso, S. Biamino, P. Minetola, D. Manfredi, *Adv. Eng. Mater.* **2017**, *19*, 1.

[27] B. Zhang, G. Bi, Y. Chew, P. Wang, G. Ma, Y. Liu, S.K. Moon, *Appl. Surf. Sci.* **2019**.

[28] Y. Huang, M. Ansari, H. Asgari, M.H. Farshidianfar, D. Sarker, M.B. Khamesee, E. Toyserkani, *J. Mater. Process. Technol.* **2019**.

[29] R. Mehrabian, *Int. Met. Rev.* **1982**.

[30] H.A. Davies, N. Shohoji, D.H. Warrington, in *2nd Int. Conf. Rapid Solidif. Process.* (Eds: R. Mehrabian, B.H. Kear, M. Cohen), Claitor's Publishing Division, Baton Rouge, LA., Reston, VA**1980**, 153.

[31] C.C. Silva, V.H.C. de Albuquerque, E.M. Miná, E.P. Moura, J.M.R.S. Tavares, *Metall. Mater. Trans. A Phys. Metall. Mater. Sci.* **2018**.

[32] B. Dubiel, J. Sieniawski, *Materials (Basel).* **2019**.

[33] D. Verdi, M.A. Garrido, C.J. Múnez, P. Poza, *Mater. Des.* **2017**.

[34] In *Metallogr. Microstruct.*, ASM International**2004**, 820.

[35] C. Thomas, P. Tait, *Int. J. Press. Vessel. Pip.* **1994**.

[36] S. Floreen, G.E. Fuchs, W.J. Yang, in *Superalloys 718, 625, 706 Var. Deriv.*, **1994**, 13.

[37] M. Rombouts, G. Maes, R. Persoons, in *Innov. Dev. Virtual Phys. Prototyp.*, CRC Press**2011**, 333.

[38] C.C. Silva, H.C. De Miranda, M.F. Motta, J.P. Farias, C.R.M. Afonso, A.J. Ramirez, *J. Mater. Res. Technol.* **2013**, *2*, 228.

[39] K. Chandrasekaran, N.S. Tiedje, J. Hald, *Int. J. Cast Met. Res.* **2009**, *22*, 306.

[40] J.. DuPont, C.. Robino, *Scr. Mater.* **1999**, *41*, 449.

[41] D.J. Kurz, W. and Fisher, *Fundamentals of Solidification*, **1998**.

[42] M.J. Cieslak, G.A. Knorovsky, T.J. Headley, A.D. Romig, Jr, *Superalloy 718 - Metall. Appl.* **1989**, 59.